Transient Stability Analysis and Enhancement of Inverter-Based Microgrid Considering Current Limitation

Dashuang Li, *Graduate Student Member, IEEE*, Qiuye Sun, *Senior Member, IEEE*, Rui Wang, *Senior Member, IEEE*, and Zhengqi Sui

***Abstract*—Affected by the current limitation, grid-forming inverters (GFMs) will transition to a current source under grid faults, which makes the inverter-based microgrid lose the voltage support and then be switched to a current source interconnection microgrid (CSIM). It may deteriorate the system's transient synchronization stability (TSS). This issue has not been studied previously. To this end, this article proposes an analysis and enhancement method of TSS of CSIM. First, a large signal synchronization model of CSIM is derived, which takes into account the effect of the current limitation strategy of GFMs and the dynamic interactions between GFMs and grid-following inverters (GFLs). Second, by constructing the Lyapunov energy function, the criterion of TSS is obtained and the impacts of parameters on stability are investigated. Based on the stability criterion, the feasible region of current references of GFLs is clearly described. Therefore, a dynamic current control method of GFLs is proposed. It can well address the absence of equilibrium points (EPs) and strengthen the transient stability. Meanwhile, a novel antiwindup strategy of GFMs considering synchronization stability constraint is proposed, which can contribute to the fault recovery of GFMs. Finally, simulation and experimental results verify the effectiveness of the proposed methods.**

***Index Terms*—Current limitation, current source interconnection microgrid (CSIM), Lyapunov energy function, transient stability analysis.**

Nomenclature

ADR	Attraction domain's radius.
CSM	Current source model.
CSIM	Current source interconnection microgrid.
EP	Equilibrium point.
FRCR	Feasible region of current references.
GFL	Grid-following inverters.
GFM	Grid-forming inverters.
IMG	Inverter-based microgrid.
LVRT	Low-voltage ride through.
PCC	Point of common connection.
PLL	Phase-locked loop.
TSS	Transient synchronization stability.
VSM	Voltage source model.

Received 23 April 2024; revised 8 July 2024 and 15 August 2024; accepted 20 September 2024. Date of publication 24 September 2024; date of current version 12 December 2024. This work was supported by the National Natural Science Foundation of China under Grant U20A20190. Recommended for publication by Associate Editor F. Azcondo. *(Corresponding author: Qiuye Sun.)*

The authors are with the College of Information Science and Engineering, Northeastern University, Shenyang 110819, China (e-mail: 2210276@stu.neu.edu.cn; sunqiuye@ise.neu.edu.cn; wangrui@ise.neu.edu.cn; 2110260@stu.neu.edu.cn).

Color versions of one or more figures in this article are available at https://doi.org/10.1109/TPEL.2024.3467215.

Digital Object Identifier 10.1109/TPEL.2024.3467215

I. Introduction

POWER electronic inverters have been widely applied in microgrids due to their efficient conversion and flexible control of electricity [1], [2], which can be classified into GFLs and GFMs according to their control methods [3], [4]. GFMs are considered a promising solution for future inverter-dominated microgrids as they participate in the regulation of voltage and frequency [5]. However, compared to synchronous generators, GFMs can only handle a few percent of overcurrent 20%–40% [6]. Therefore, GFMs usually use current limiters to limit the output currents [7]. Nevertheless, current limiters may have adverse effects on TSS in grid-connected GFMs [8].

In order to limit the output currents during faults, two typical control strategies have been proposed for GFMs [9], [10], [11], [12]. One strategy is the current saturation algorithm, which directly restricts the current reference [9], [10]. Another strategy is the virtual impedance method, which modifies the voltage control reference by adding virtual impedance [11], [12]. In [13], comparative studies between these two strategies in the case of a three-phase short circuit are performed, which reveals that the current saturation algorithm has a better performance in limiting the output currents during the first milliseconds after faults. Therefore, the current saturation algorithm is adopted as the current-limiting method of GFMs in this article.

The output of GFLs and GFMs present current source and voltage-source characteristics, respectively [14]. GFLs can still operate in the CSM even though the current limiter saturates during faults [15]. However, affected by the current limiter, GFMs will be switched from the VSM to the CSM during faults [10]. The mode switching will make the IMG lose the voltage support and then be switched to a CSIM, which may deteriorate the system TSS.

The transient instability mechanism of GFMs with current limiters has been studied [16], [17], [18], [19], [20]. The TSS of virtual synchronous generator-controlled GFM with current limiters is analyzed based on the Lyapunov energy function [16]. The transient stability of droop-controlled GFM considering

current limitation is investigated using the virtual power angel curve [10]. The impact of the current reference angle on the transient stability of GFM is also studied, and the optimal value is derived [17]. The steady-state angle stability of parallel GFMs in CSM is investigated, which reveals that the angle stability under inductive load is opposite to that under capacitive load [18]. However, these studies consider the GFM as a single unit tied to an infinite bus, the dynamic interactions among different types of inverters are not considered. In [19], the fault recovery process of GFMs with current limiters is analyzed, and three post-fault scenarios are defined. When GFMs exit CSM, the current reference is generated again by the voltage control loop. The windup effect of the integrator will cause GFMs to be unable to recover from faults successfully, resulting in system instability. Although the traditional antiwindup methods relieve the saturation effect of the PI regulator by limiting the output or performing conditional integration [20], they cannot eliminate the impact of the sudden changes in the difference between the voltage reference and the measurement on the fault recovery of GFMs.

GFLs depend on PLLs for synchronization with the power grid [21], [22]. PLLs may suffer loss of synchronization if the active current reference of GFLs exceeds the transfer capacity [23]. Generally, there are two requirements for the synchronous stability, i.e., the existence of a stable EP and the system states converging to the stable EP [24]. The transient stability analysis of GFLs has been investigated by using the equal area criterion method [25], [26] and Lyapunov direct method [27], [28]. However, these works consider the inverters as a single unit tied to an infinite bus. To improve the transient stability of GFLs, a variable structure PLL method is proposed, which freezes the integral regulator and remains the proportional regulator of PLL during faults [29]. A voltage regulation control method is proposed to adjust the PLL's input during faults by adding a q-axis component of the grid-connected voltage [30]. However, the above strategies cannot ensure the system's transient stability in the absence of EPs. To ensure the existence of stable EPs during faults, a voltage-dependent current control method is proposed [24]. However, it studies the synchronization stability between GFLs and the grid, which does not consider the effect of GFMs.

In IMG, when GFMs are switched from VSM to CSM under grid faults, the system will lose the voltage support and then be switched to a CSIM. The system voltage is determined by the output current of GFMs and GFLs and network impedance, which is very weak and susceptible. The TSS of CSIM is more severe and complex. Nevertheless, to the best of our knowledge, the corresponding transient synchronization instability mechanism has not been theoretically explored in the literature so far.

To fill this gap, this article conducts the TSS analysis and enhancement method of the CSIM. The main contributions are summarized as follows.

1) The large signal synchronization model of CSIM is derived for the first time, which takes into account the effect of the current limitation strategy of GFMs and the dynamic interactions between GFMs and GFLs. Based on the synchronization model, the Lyapunov energy function of CSIM is established. Then, the criterion of TSS is obtained and the FRCRs of GFLs is derived. Meanwhile, the impacts of parameters on system stability are investigated.
2) Based on the stability criterion, a dynamic current control method of GFLs is proposed, which adjusts the active current reference and reactive current reference of GFLs to address the absence of EPs and strengthen the transient stability.
3) A novel antiwindup strategy of GFMs considering synchronization stability constraint is proposed, which dynamically adjusts the voltage reference of GFMs in the process of fault recovery, and freezes the integrator when GFMs operate in CSM. It is useful for GFMs exiting CSM and fault recovery.

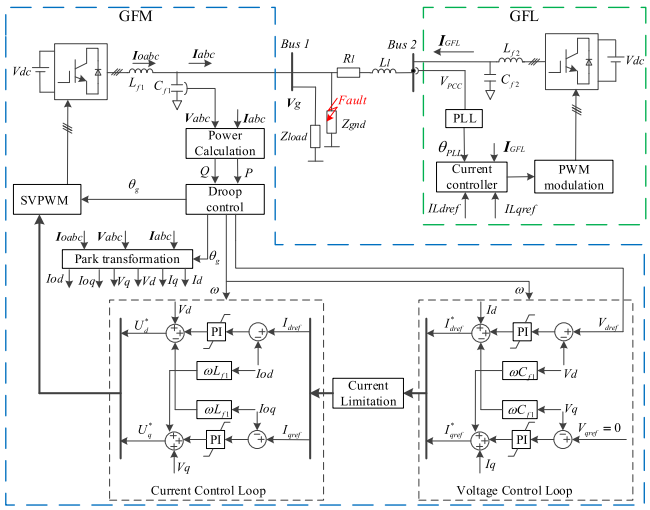

Fig. 1. Structure diagram of IMG.

The rest parts of this article are organized as follows. The large signal synchronization model of CSIM is derived in Section II. The transient synchronous stability is analyzed in Section III. In Section IV, control strategies for enhancing transient stability are proposed. To illustrate the effectiveness and superiority of the proposed method, simulation, and experimental results are presented in Sections V and VI respectively. Section VII concludes the article.

II. Large Signal Synchronization Model of CSIM

An IMG is shown in Fig. 1, concluding a GFM, a GFL, and a loads Z_{load}. L_{f1} and L_{f2} are the filter inductance of the inverters, C_{f1} and C_{f2} are the filter capacitor of the inverters, R_l is the line resistance, L_l is the line inductance. The control structure of the GFM is also shown in Fig. 1.

In this article, the d-axis priority-based current limitation strategy is adopted for the GFM, which is commonly used and easy for implementation [31]. This strategy is described as follows:

$$\begin{cases} |I_{d\text{ref}}| = \min(I_{\max}, |I_{d\text{ref}}{}^*|) \\ |I_{q\text{ref}}| = \min(\sqrt{(I_{\max})^2 - (I_{d\text{ref}})^2}, |I_{q\text{ref}}{}^*|) \end{cases} \tag{1}$$

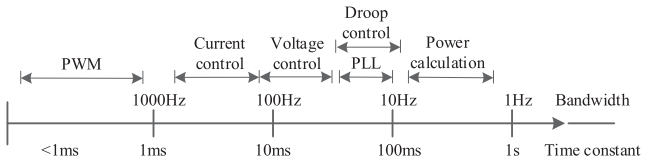

Fig. 2. Characteristic timescales of different control loops.

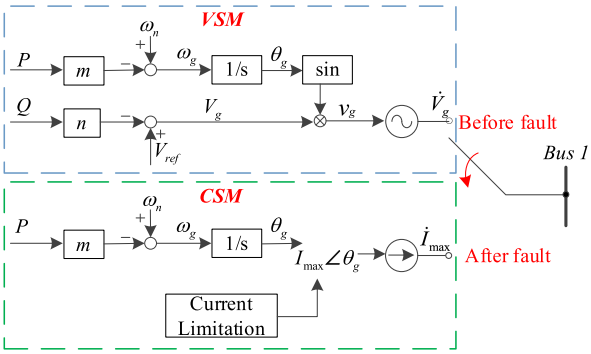

Fig. 3. Control structure of the GFM under mode switching.

where I^*_{dref} and I^*_{qref} are the outputs of voltage control loop, $I_{\max}$ is the maximum allowable current magnitude.

A. Equivalent Model of the GFM

As shown in Fig. 1, the control structure of the GFM consists of droop control loop, voltage control loop, and current control loop. In general, as shown in Fig. 2, the voltage and current control loops respond faster than the P-f droop control loop [32], [33]. The dynamics of the voltage and current control loops can be ignored in the transient stability analysis since the transient stability of the GFM is dominated by the P-f droop control [8].

Ignoring these factors is to facilitate the explanation of the transient stability mechanism of GFMs. All the factors are fully considered in the simulations and experiments to validate the effectiveness of the transient stability analysis and the proposed enhancement control strategy based on the equivalent model.

When the GFM operates in the VSM, the frequency and voltage are regulated by the P-f and Q-V droop control. When the GFM operates in the CSM, the frequency and current are regulated by the P-f droop control and the current limitation link. The equivalent model is given in Fig. 3.

B. Equivalent Model of the GFL

As known, the dynamic characteristic of the GFL behaves as a current source, which has a fast response for power supply. Therefore, the output current of the GFL is $i_{\text{GFL}} = I_{\text{GFL}}\angle(\theta_{\text{PLL}} + \varphi)$, where $\varphi = \arctan(i_{Lq}/i_{Ld})$, i_{Ld} and i_{Lq} are the d-axis and q-axis components of i_{GFL}, respectively. The synchronous reference frame PLL is commonly adopted for the GFL [21], which is shown in Fig. 4. Also, the dynamics of the current controller are much faster than the PLL's dynamics, its dynamics are neglected, and the current controller is supposed ideal [27].

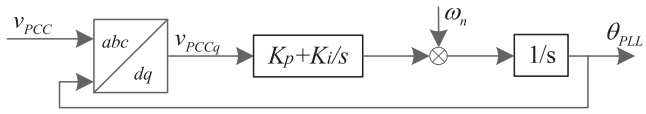

Fig. 4. PLL structure of the GFL.

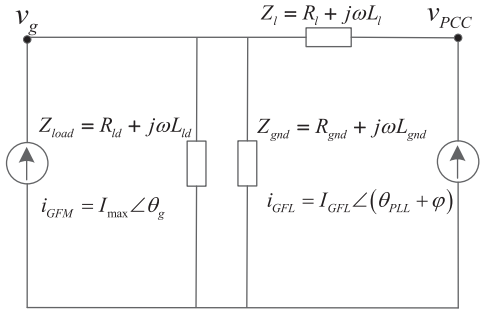

Fig. 5. Equivalent circuit of CSIM.

C. Equivalent Circuit of CSIM

When GFMs transition to CSM under grid faults, the IMG shown in Fig. 1 becomes a CSIM. Based on the previous analysis, the equivalent circuit of CSIM is shown in Fig. 5.

According to Kirchhoff's law, the voltages at the Bus 1 v_g and the PCC of the GFL v_{PCC} are expressed in (2) and (3), respectively

$$v_g = Z_{\text{lg}}(\omega_g) i_{\text{GFM}} + Z_{\text{lg}}(\omega_{\text{PLL}}) i_{\text{GFL}} \tag{2}$$

$$v_{\text{PCC}} = Z_{\text{lg}}(\omega_g) i_{\text{GFM}} + \left[Z_l(\omega_{\text{PLL}}) + Z_{\text{lg}}(\omega_{\text{PLL}})\right] i_{\text{GFL}} \tag{3}$$

where $Z_{\text{lg}} = Z_{\text{load}} // Z_{gnd}$. ω_g and ω_{PLL} are the angular speed of droop control of the GFM and PLL of the GFL, respectively. At the steady state, $\omega_g = \omega_{\text{PLL}}$.

By applying the d-q frame transformation, (2) and (3) can be written in the PLL reference frame as

$$\begin{cases} v_{gd} = R_{lg} I_{\max} cos\left(\theta_{\text{PLL}} - \theta_g\right) + X_{lg} I_{\max} \sin\left(\theta_{\text{PLL}} - \theta_g\right) \\ \qquad + R_{lg} i_{ld} - X_{lg} i_{lq} \\ v_{gq} = X_{lg} I_{\max} cos\left(\theta_{\text{PLL}} - \theta_g\right) - R_{lg} I_{\max} \sin\left(\theta_{\text{PLL}} - \theta_g\right) \\ \qquad + X_{lg} i_{ld} + R_{lg} i_{lq} \end{cases} \tag{4}$$

$$\begin{cases} v_{\text{PCC}d} = R_{lg} I_{\max} cos\left(\theta_{\text{PLL}} - \theta_g\right) + X_{lg} I_{\max} \sin\left(\theta_{\text{PLL}} - \theta_g\right) \\ \qquad + \left(R_{lg} + R_l\right) i_{ld} - \left(X_{lg} + X_l\right) i_{lq} \\ v_{\text{PCC}q} = X_{lg} I_{\max} \cos\left(\theta_{\text{PLL}} - \theta_g\right) - R_{lg} I_{\max} \sin\left(\theta_{\text{PLL}} - \theta_g\right) \\ \qquad + \left(X_{lg} + X_l\right) i_{ld} + \left(R_{lg} + R_l\right) i_{lq} \end{cases} \tag{5}$$

where v_{gd} and v_{gq} are the d-axis and q-axis components of v_g, respectively; $v_{\text{PCC}d}$, $v_{\text{PCC}q}$ are the d-axis and q-axis components of v_{PCC}, respectively; θ_g and θ_{PLL} are the angle of v_g and PLL, respectively. $R_{\text{lg}} = \text{Re}(Z_{\text{lg}})$, $X_{\text{lg}} = \text{Im}(Z_{\text{lg}})$.

According to the Fig. 4, the dynamic of PLL can be expressed as follows:

$$\theta_{PLL} = \int_0^t \left[\omega_n + K_p v_{PCCq} + K_i \int_0^t v_{PCCq} dt\right] dt \tag{6}$$

where ω_n is the nominal angular speed, K_p and K_i are the PI parameters of PLL.

The dynamic equation of ω_{PLL} is derived based on (6), in which $L = L_{\mathrm{l}} + X_{\mathrm{lg}}/\omega_{\mathrm{PLL}}$.

According to the equivalent circuit of CSIM in Fig. 5, the output active power of the GFM P_{GFM} is calculated as follows:

$$P_{\mathrm{GFM}} = 1.5\left[R_{lg}I_{\max}^2\cos\left(\theta_{\mathrm{PLL}}-\theta_g\right) + X_{lg}I_{\max}^2\sin\left(\theta_{\mathrm{PLL}}-\theta_g\right) + R_{lg}i_{ld}I_{\max} - X_{lg}i_{lq}I_{\max}\right]. \tag{8}$$

The angular speed ω_g of the GFM is represented according to the droop control method in Fig. 3

$$\begin{aligned}\omega_g &= \omega_n - mP_{\mathrm{GFM}}\\ &= \omega_n\\ &- 1.5\cdot m\begin{bmatrix}R_{lg}I_{\max}^2\cos\left(\theta_{\mathrm{PLL}}-\theta_g\right) + X_{lg}I_{\max}^2\sin\left(\theta_{\mathrm{PLL}}-\theta_g\right)\\ +R_{lg}i_{ld}I_{\max} - X_{lg}i_{lq}I_{\max}\end{bmatrix}\end{aligned} \tag{9}$$

where m is the active power droop coefficient.

According to (7) shown at the bottom of this page, and (9), there exists frequency interactions between GFMs and GFLs. The dynamic equations of frequency are entirely determined by the current outputs of GFMs and GFLs, as well as the system impedance. The TSS of CSIM is more severe and complex.

D. State-Space Model of CSIM

The system states of CSIM are defined as follows:

$$\begin{cases}x_1 = \theta_{PLL} - \theta_g\\ x_2 = \omega_{PLL} - \omega_g\end{cases}. \tag{10}$$

According to (7) and (9), the state-space model of CSIM is constructed

$$\begin{cases}\dot{x}_1 = x_2\\ M\dot{x}_2 = A - B\sin\left(x_1+\varphi_1\right) - Dx_2\end{cases} \tag{11}$$

where

$$\begin{cases}M = 1-K_pLi_{ld}\\ A = \left[K_iLi_{ld}\left(\omega_n + 1.5mX_{lg}i_{lq}I_{\max} - 1.5mR_{lg}i_{ld}I_{\max}\right)\right.\\ \quad\left. + K_i\left(R_{lg}+R_l\right)i_{lq}\right]\\ B = \sqrt{k_1^2+k_2^2};\ D = k_3 + \sqrt{k_4^2+k_5^2}\sin\left(x_1+\varphi_2\right)\\ k_1 = \left(K_iR_{\mathrm{lg}}I_{\max} + 1.5K_iLi_{ld}mX_{lg}I_{\max}^2\right)\\ k_2 = \left(K_iX_{lg}I_{\max} - 1.5K_iLi_{ld}mR_{lg}I_{\max}^2\right)\\ k_3 = -K_iLi_{ld}\\ k_4 = K_pX_{lg}I_{\max} + 1.5mR_{lg}I_{\max}^2M^2\\ k_5 = K_pR_{lg}I_{\max} - 1.5mX_{lg}I_{\max}^2M^2\\ \varphi_1 = -\arctan\left(k_2/k_1\right),\varphi_2 = \arctan\left(k_5/k_4\right)\end{cases}$$

TABLE I
SIMULATION SYSTEM PARAMETERS

Parameters	Description	Value
V_{dc}	DC link voltage	800 V
m_i	Active power droop coefficient	1e-4
n_i	Reactive power droop coefficient	1e-4
L_{f1}, L_{f2}	Filter inductance of inverter	2 mH,1 mH
C_{f1}, C_{f2}	Filter capacitor of inverter	50 uF,20 uF
R_l	line resistance	5.233 Ω
L_l	line inductance	50 mH
V_g	voltage magnitude of GFM	311 V
ω_n	Rated angular speed	314 rad/s
K_p, K_i	*PI* parameters of PLL	0.37, 9.9
Z_{load}	Load power	28.88 Ω
R_{gnd}	grounding resistance	5 Ω
I_{max}	maximum output current of GFM	25 A

The EPs of CSIM can be obtained by setting $\dot{x}_1 = 0, \dot{x}_2 = 0$

$$\begin{aligned}\left(x_1^e, x_2^e\right) &= \left(\sin^{-1}\left(A/B\right) - \varphi_1, 0\right), or\ \left(x_1^e, x_2^e\right)\\ &= \left(\pi - \sin^{-1}\left(A/B\right) + \varphi_1, 0\right).\end{aligned} \tag{12}$$

Making $x_1 = \tilde{x}_1 + \beta, x_2 = \tilde{x}_2$, the state-space model of CSIM can be rewritten as

$$\begin{cases}\dot{\tilde{x}}_1 = \tilde{x}_2 = f_1\left(\tilde{x}_1, \tilde{x}_2\right)\\ M\dot{\tilde{x}}_2 = A - B\sin\left(\tilde{x}_1+\beta+\varphi_1\right) - D_{eq}\tilde{x}_2 = f_2\left(\tilde{x}_1, \tilde{x}_2\right)\end{cases} \tag{13}$$

where

$$D_{\mathrm{eq}} = k_3 + \sqrt{k_4^2+k_5^2}\sin\left(\tilde{x}_1+\beta+\varphi_2\right)$$

$$\beta = \left(\sin^{-1}\left(A/B\right) - \varphi_1, 0\right), or\ \left(\pi - \sin^{-1}\left(A/B\right) + \varphi_1, 0\right).$$

E. Accuracy Verification of the CSIM Model

The effectiveness and accuracy of the modeling method can be validated by comparing the dynamic characteristics of the math model and the simulation model under a large disturbance. An IMG shown in Fig. 1 is established using MATLAB/Simulink. The system parameters are given in Table I.

The active current reference of the GFL $I_{Ld\mathrm{ref}}$ steps from 2 to 6 A at $t = 0.4$ s. The simulation results are shown in Fig. 6. As shown in Fig. 6, the trend of the response curves of the math model in (11) and the simulation model is the same, and the deviation is very small. The average errors of the math model in Fig. 6(a) and (b) are about 0.97% and 1.55%, and the maximum errors are about 7.9% and 10.3%, respectively.

$$\ddot{\theta}_{\mathrm{PLL}} = \frac{\begin{array}{l}-K_iR_{\mathrm{lg}}I_{\max}\sin\left(\theta_{\mathrm{PLL}}-\theta_g\right) + K_iX_{\mathrm{lg}}I_{\max}\cos\left(\theta_{\mathrm{PLL}}-\theta_g\right)\\ -\left[K_pR_{lg}I_{\max}\cos\left(\theta_{\mathrm{PLL}}-\theta_g\right) + K_pX_{lg}I_{\max}\sin\left(\theta_{\mathrm{PLL}}-\theta_g\right)\right]\left(\omega_{\mathrm{PLL}}-\omega_g\right)\\ +K_i\left(R_{lg}+R_l\right)i_{lq} + K_i\omega_{\mathrm{PLL}}Li_{ld}\end{array}}{1-K_pi_{ld}L}. \tag{7}$$

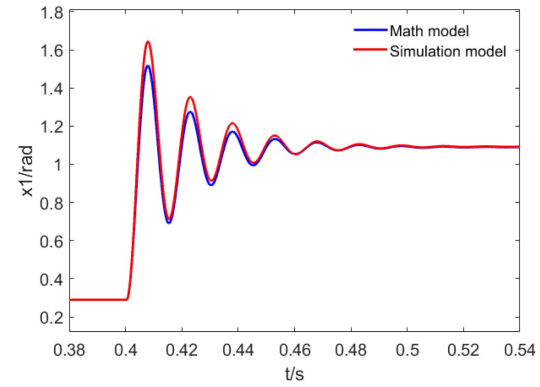

(a)

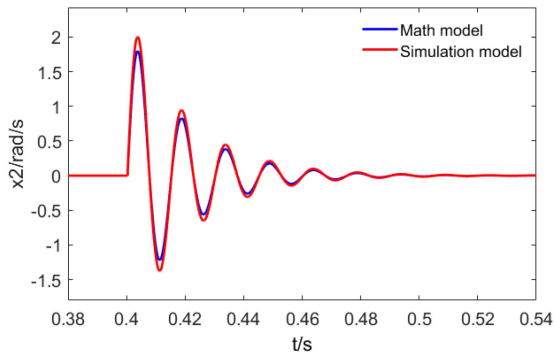

(b)

Fig. 6. Response curves of the math model and the simulation model under a large disturbance. (a) State variable x1. (b) State variable x2.

III. Transient Synchronous Stability Analysis of CSIM

A. Stability Analysis of EP

The Jacobian matrix of the state space model of CSIM shown as (13) is calculated as follows:

$$J = \left(\begin{array}{cc} \frac{\partial f_1(\tilde{x}_1,\tilde{x}_2)}{\partial \tilde{x}_1}, & \frac{\partial f_1(\tilde{x}_1,\tilde{x}_2)}{\partial \tilde{x}_2} \\ \frac{\partial f_2(\tilde{x}_1,\tilde{x}_2)}{\partial \tilde{x}_1}, & \frac{\partial f_2(\tilde{x}_1,\tilde{x}_2)}{\partial \tilde{x}_2} \end{array} \right)_{|} \quad \tilde{x}_1 = 0, \tilde{x}_2 = 0$$

$$= \left(\begin{array}{cc} 0, & 1 \\ -B\cos(\beta+\varphi_1), & -D_{\text{eq}|\tilde{x}_1=0} \end{array} \right) \tag{14}$$

According to (14), the Jacobian matrix's determinant is obtained as follows:

$$det(\lambda I - J) = \left| \begin{array}{cc} \lambda, & -1 \\ B\cos(\beta+\varphi_1), & \lambda + D_{\text{eq}|\tilde{x}_1=0} \end{array} \right|. \tag{15}$$

Thus, the characteristic equation is as follows:

$$\lambda^2 + D_{\text{eq}|\tilde{x}_1=0}\lambda + B\cos(\beta+\varphi_1) = 0. \tag{16}$$

Hence, the stability conditions of EPs are

$$D_{eq|\tilde{x}_1=0} > 0 \tag{17}$$

$$B\cos(\beta+\varphi_1) > 0. \tag{18}$$

According to (18), the first EP is stable. The second one is unstable. And (18) is always satisfied at first EP. According to (17) and expressions of β and φ_2, the stability condition of EPs is as follows:

$$-k_3 - \sqrt{k_4^2 + k_5^2}\frac{\sqrt{B^2 - A^2}}{B} < 0. \tag{19}$$

According to (19), the condition for existence of EPs in CSIM is $|A| < B$. Therefore, the output current of GFLs should be smaller than a certain value. Since A and B are functions of system different variables, other variables also have an impact on the existence of EPs, such as the PLL dynamics and current limitation strategy. Equation (19) provides a quantitative expression of variables for having a stable EP. Based on this, the design principles of system parameters are given.

B. Attraction Domain of EP

The attraction domain of EPs is a set of initial values of the states that converge to the EP, which is an important attribute of a nonlinear system.

Owing to the lack of a systematic method for constructing Lyapunov's function for a nonlinear system, Lyapunov's function can be established based on the state-space model of CSIM shown as (13). The construction principle is to find the sufficient and necessary condition that makes $\dot{V}(\tilde{x})$ negative definite [34]. First, Lyapunov's function should include all states of CSIM. Thus, $M\tilde{x}_2^2/2$ is chosen according to the expression of Lyapunov's function of power grid. $M\tilde{x}_2\dot{\tilde{x}}_2$ is obtained by taking the above term's derivative, which is $A\tilde{x}_2 - B\sin(\tilde{x}_1+\beta+\varphi_1)\tilde{x}_2 - D_{\text{eq}}\tilde{x}_2^2$. As we known, the sign of $-D_{eq}\tilde{x}_2^2$ depends on $-D_{eq}$. At the EP of CSIM, the above expression becomes $-D_{eq|\tilde{x}_1=0}$, which is negative when the stability conditions of EPs shown as (17) are met. Then, the remaining terms in the Lyapunov's function are constructed to offset the remaining terms in $\dot{V}(\tilde{x})$, i.e., $A\tilde{x}_2 - B\sin(\tilde{x}_1+\beta+\varphi_1)\tilde{x}_2$. In order to offset $A\tilde{x}_2$ and $-B\sin(\tilde{x}_1+\beta+\varphi_1)\tilde{x}_2$, $-A\tilde{x}_1$ and $-B\cos(\tilde{x}_1+\beta+\varphi_1)$ are included to $V(\tilde{x})$. Furthermore, the value of a Lyapunov's function should be equal to zero at the origin. Therefore, $B\cos(\alpha+\varphi_1)$ is included to $V(\tilde{x})$ to satisfy the above requirement.

Therefore, the Lyapunov's function is established as follows:

$$V(\tilde{x}) = M\tilde{x}_2^2/2 - A\tilde{x}_1 - B[\cos(\tilde{x}_1+\beta+\varphi_1) - \cos(\beta+\varphi_1)]. \tag{20}$$

To prove the above function is a suitable Lyapunov's function, there should exist neighborhood (W_1) and neighborhood (W_2) around the EP in which

$$\begin{cases} V(\tilde{x}) > 0 \ \forall \tilde{x} \in W_1 - \{0\}, and, V(\tilde{x}) = 0 \\ \dot{V}(\tilde{x}) < 0 \ \forall \tilde{x} \in W_2 - \{0\} \end{cases}. \tag{21}$$

The expressions of W_1 and W_2 are obtained as follows. The derivation is given in Appendix A

$$W_1 = \left[-\pi - 2\sin^{-1}(A/B), \pi - 2\sin^{-1}(A/B)\right] \tag{22}$$

$$W_2 = \begin{bmatrix} \sin^{-1}\left(-k_3/\sqrt{k_4^2+k_5^2}\right) - \sin^{-1}(A/B) + (\varphi_1 - \varphi_2), \\ \pi - \sin^{-1}\left(-k_3/\sqrt{k_4^2+k_5^2}\right) - \sin^{-1}(A/B) + (\varphi_1 - \varphi_2) \end{bmatrix}. \tag{23}$$

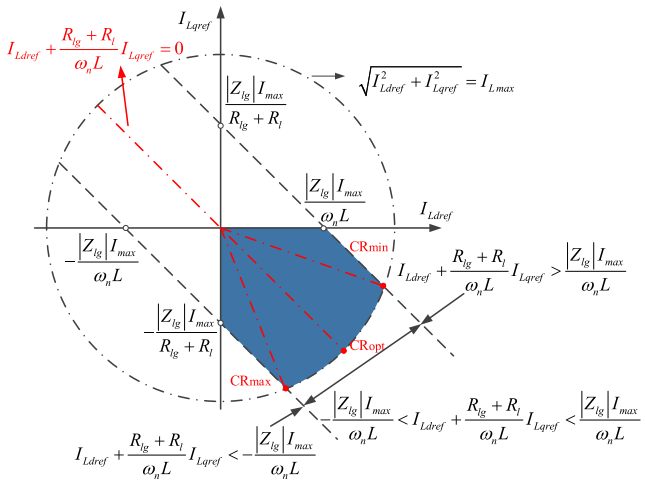

Fig. 7. FRCR of the GFL.

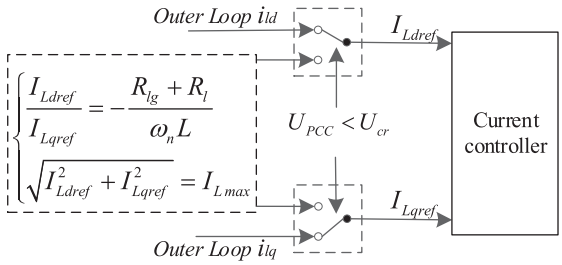

Fig. 8. Proposed dynamic current control method.

When considering pure active power loads and metallic short circuit faults, i.e., $X_{\mathrm{lg}}=0$, then $\varphi_1\approx 0$ and $\varphi_2\approx \pi/2$. Equation (23) can be rewritten as follows:

$$W_2=\begin{bmatrix}-\pi/2+\sin^{-1}\left(-k_3/\sqrt{k_4^2+k_5^2}\right)-\sin^{-1}(A/B),\\ \pi/2-\sin^{-1}\left(-k_3/\sqrt{k_4^2+k_5^2}\right)-\sin^{-1}(A/B)\end{bmatrix}. \tag{24}$$

The positive definite of (20) and the semi-negative definite of its time derivative have been proved, which indicates that (20) is a suitable Lyapunov's function and can be used to analyze the transient stability of the CISM.

According to the Lassale theorem, the origin is asymptotically stable in $W_1\cap W_2$ [35]. The attraction domain of EPs is as follows:

$$V(\tilde{x})>0 \text{ and } \dot{V}(\tilde{x})<0,$$
$$\forall\tilde{x}_1\in\begin{bmatrix}-\pi/2+\sin^{-1}\left(-k_3/\sqrt{k_4^2+k_5^2}\right)-\sin^{-1}(A/B),\\ \pi/2-\sin^{-1}\left(-k_3/\sqrt{k_4^2+k_5^2}\right)-\sin^{-1}(A/B)\end{bmatrix}-\{0\}. \tag{25}$$

According to (25), the ADR is obtained as follows:

$$r=\pi/2-\sin^{-1}\left(-k_3/\sqrt{k_4^2+k_5^2}\right)-\sin^{-1}(A/B). \tag{26}$$

According to (26), reducing the values of i_{ld} and K_i, increasing the values of i_{lq} and K_p will increase the value of r, namely, improve the system transient stability. Therefore, the value of r reflects the system strength, which can be used to evaluate system strength. If $r=0$, it corresponds to an unstable system; if $0<r<\pi/2$, it corresponds to a stable system. The larger the value of r is, the stronger the system strength is.

C. FRCR of the GFL

The definition of the FRCR is as follows: the feasible region of active current reference $I_{Ld\mathrm{ref}}$ and reactive current reference $I_{Lq\mathrm{ref}}$ of the GFL are the values to ensure the transient stability of the CISM. If the GFL operates under the unity power factor, and m is very small, the active current reference is obtained as follows according to (19):

$$I_{Ld\mathrm{ref}}<I_{\max}\sqrt{R_{lg}^2+X_{lg}^2}/\left(L\sqrt{(K_{\mathrm{i}}/K_p)^2+\omega_n^2}\right). \tag{27}$$

However, according to the Chinese LVRT grid code, the GFL should inject reactive current to support voltage recovery during faults [36]. According to (19), the condition of the active current reference $I_{Ld\mathrm{ref}}$ and reactive current reference $I_{Lq\mathrm{ref}}$ of the GFL for the EP to be stable is as follows:

$$\left[1+\left(\frac{K_i}{K_p}\right)^2\frac{1}{\omega_n^2}\right]I_{Ld\mathrm{ref}}^2+2\frac{R_{lg}+R_l}{\omega_n L}I_{Ld\mathrm{ref}}I_{Lq\mathrm{ref}}+\left(\frac{R_{lg}+R_l}{\omega_n L}\right)^2I_{Lq\mathrm{ref}}^2<\frac{|Z_{lg}|^2I_{\max}^2}{(\omega_n L)^2}. \tag{28}$$

Because the value of $(K_i/K_p)^2/\omega_n^2$ is small, (28) can be rewritten as follows:

$$\left(I_{Ld\mathrm{ref}}+\frac{R_{lg}+R_l}{\omega_n L}I_{Lq\mathrm{ref}}\right)^2<\frac{|Z_{lg}|^2I_{\max}^2}{(\omega_n L)^2}. \tag{29}$$

During faults, $i_{ld}\geq 0$ and $i_{lq}<0$ [23]. Based on (29), the FRCR of the GFL during faults is calculated as shown in the blue area in Fig. 7, in which $|Z_{lg}|=\sqrt{R_{lg}^2+X_{lg}^2}$ and $I_{L\max}$ is the maximum output current of the GFL. The FRCR of the GFL will shrink due to the fault deterioration and weakening of system strength, i.e., the decrease of Z_{lg} and the increase of L. In this condition, the current reference of the GFL might be out of the FRCR, causing EP nonexistent and incurring loss of synchronization.

According to the FRCRs of GFLs shown in Fig. 7, the optimal current ratio (CR) of active current reference to reactive current reference is $\mathrm{CR}_{\mathrm{opt}}=-(R_{\mathrm{lg}}+R_{\mathrm{l}})/\omega_{\mathrm{n}}L$. And the maximum value $\mathrm{CR}_{\max}$ and minimum value $\mathrm{CR}_{\min}$ of CR can be obtained by solving (30) and (31) shown as follows, respectively. The CR should be in the range $[\mathrm{CR}_{\min}, \mathrm{CR}_{\max}]$ to ensure the system's stability

$$\begin{cases}I_{Ld\mathrm{ref}}+\frac{R_{lg}+R_l}{\omega_n L}I_{Lq\mathrm{ref}}+\frac{|Z_{lg}|I_{\max}}{\omega_n L}=0\\ \sqrt{I_{Ld\mathrm{ref}}^2+I_{Lq\mathrm{ref}}^2}=I_{L\max}\\ \mathrm{CR}=I_{Ld\mathrm{ref}}/I_{Lq\mathrm{ref}}\end{cases} \tag{30}$$

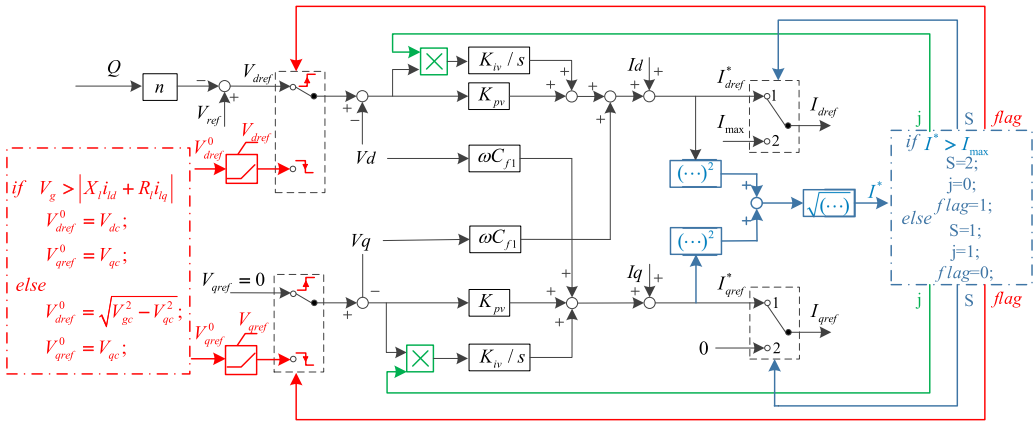

Fig. 9. Proposed antiwindup strategy.

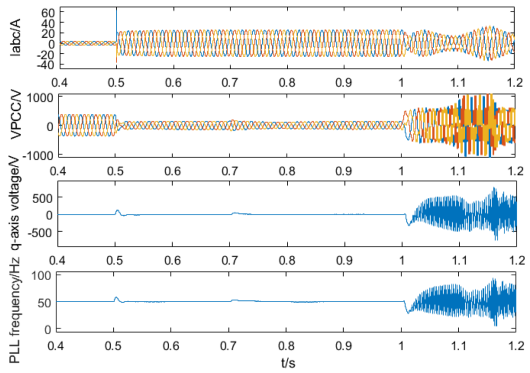

Fig. 10. Simulation results.

$$\begin{cases} I_{Ld\text{ref}} + \frac{R_{lg}+R_l}{\omega_n L} I_{Lq\text{ref}} - \frac{|Z_{lg}|I_{\max}}{\omega_n L} = 0 \\ \sqrt{I_{Ld\text{ref}}^2 + I_{Lq\text{ref}}^2} = I_{L\max} \\ \text{CR} = I_{Ld\text{ref}}/I_{Lq\text{ref}} \end{cases}. \tag{31}$$

IV. Control Strategy for Enhancing Transient Stability

A. Dynamic Current Control Method of GFLs

In IMG, GFMs will transition to the CSM from the VSM by limiting the reference of the inner current loop under conditions of overload or low voltage, which makes the IMG lose voltage source support and become a CISM. At this time, the system voltage is determined by the output currents of GFMs and GFLs, and the network impedance. However, GFLs rely on the PLL to maintain synchronization with the grid. As known from Fig. 4, the primary condition for GFLs to maintain synchronization with the grid is that the q-axis component of v_{PCC} can be set to zero. Meanwhile, as known from (5), the voltage of the CISM is determined by the output currents of GFMs and GFLs and the network impedance.

According to the TSS analysis conducted in Section III, it can be concluded that the output current of GFLs has a significant impact on the existence and stability of EPs. And according to ADR shown in (26) and the stability condition of EPs shown as (29), the system TSS is strongest when $I_{Ld\text{ref}} = -(R_{lg} + R_l)I_{Lq\text{ref}}/\omega_n L$.

Therefore, a novel dynamic current control method of GFLs is proposed to improve the TSS of the CISM, which is shown in (32). The current control block diagram of GFLs is shown in Fig. 8. If a grid fault occurs in the system, the current loop control strategy is switched to the proposed control strategy. The logic to obtain the fault flag is that the amplitude of v_{PCC} is below a certain value

$$\begin{cases} \frac{I_{Ld\text{ref}}}{I_{Lq\text{ref}}} = -\frac{R_{lg}+R_l}{\omega_n L} \\ \sqrt{I_{Ld\text{ref}}^2 + I_{Lq\text{ref}}^2} = I_{L\max} \end{cases}. \tag{32}$$

B. Novel Antiwindup Strategy of GFMs

The current limitation strategy of GFMs shown in (1) is to employ an inner current control loop and to directly limit the current reference during grid faults. While this type of method can precisely limit fault current, the latch-up and wind-up issues may happen, which challenge the fault-recovery process [18]. The failure of the fault recovery of GFMs may cause system instability.

As shown in Fig. 1, when the GFM operates in CSM, the voltage control loop is in an out-of-control state. The difference between the voltage reference and the measurement will continuously increase through the integrator. When the GFM exits CSM, the current reference is generated again by the voltage control loop. The windup effect of the integrator will cause the GFM to be unable to recover from faults successfully, resulting in system instability.

Therefore, a novel antiwindup strategy is proposed to the PI regulators in the voltage control loop of the GFM for addressing the fault recovery issue and then improving the system's transient stability. The proposed strategy is shown in Fig. 9. It mainly consists of three special function section, which are as follows.

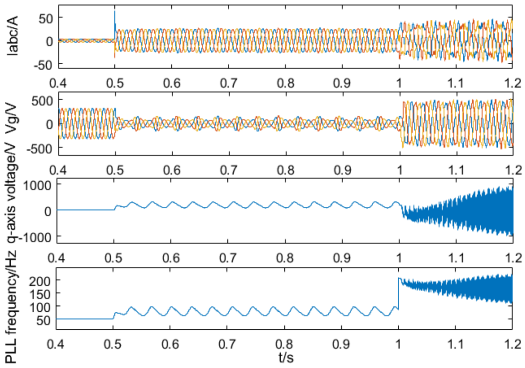

Fig. 11. Simulation results of the first strategy.

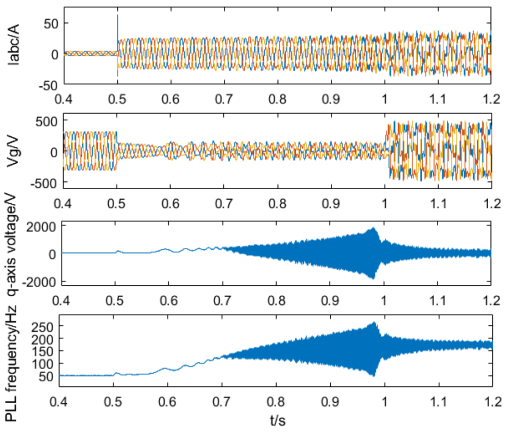

Fig. 12. Simulation results of the second strategy.

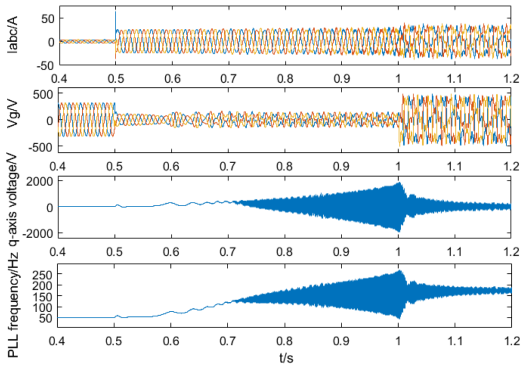

Fig. 13. Simulation results of the third strategy.

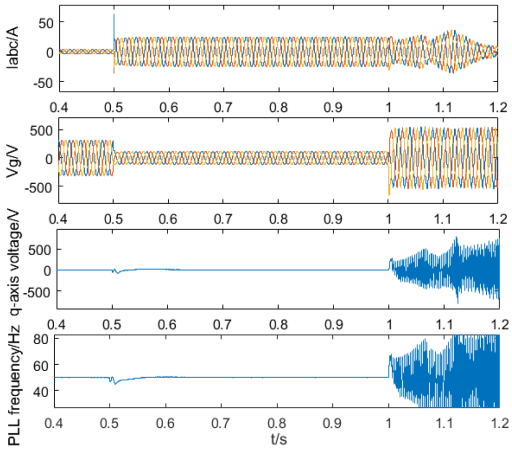

Fig. 14. Simulation results of the fourth strategy.

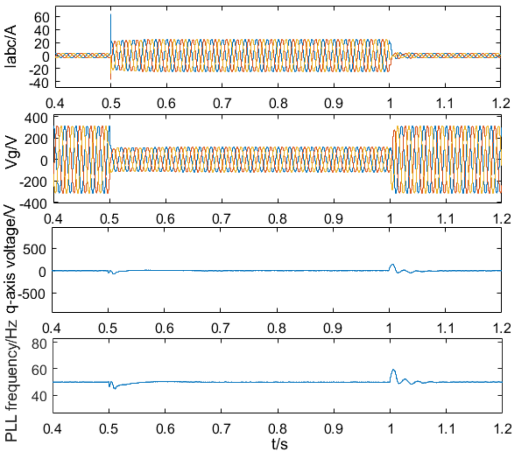

Fig. 15. Simulation results of the proposed strategy.

1) The main control section, which is highlighted in blue. It determines whether the GFM is running in normal operation or current limitation operation, and then generates corresponding control commands.
2) The integrator frozen section, which is highlighted in green. During the current limitation operation, the integrator is frozen by multiplying its input by zero.
3) The dynamic adjustment of the voltage reference section, which is highlighted in red. It generates a dynamic voltage starting from V_{ref}^0 and rising to the reference value at a certain slope. The slope can be selected based on factors such as the dynamic response speed of the PI regulators and the impact on system stability.

As shown in Fig. 1, when the GFM operates in VSM, the q-axis component of v_{PCC} is expressed as follows:

$$v_{\mathrm{PCC}q} = -V_g \sin\left(\theta_{\mathrm{PLL}} - \theta_g\right) + X_l i_{ld} + R_l i_{lq}. \tag{33}$$

The primary condition for GFL achieving synchronous stability is $v_{PCCq} = 0$ [21], i.e.

$$V_g > \left|X_l i_{ld} + R_l i_{lq}\right|. \tag{34}$$

Therefore, in order to reduce the difference between voltage reference and measurement while ensuring system synchronization stability, the principle of selection of V_{ref}^0 is as follows: *i*. if $V_g \geq V_{gc} = |X_l i_{ld} + R_l i_{lq}|$, then $V_{dref}^0 = V_{dc}, V_{qref}^0 = V_{qc}$; *ii*. if $V_g < |X_l i_{ld} + R_l i_{lq}|$, then $V_{dref}^0 = \sqrt{V_{gc}^2 - V_{qc}^2}, V_{qref}^0 = V_{qc}$, where V_{dc} and V_{qc} are the d-axis and q-axis components of v_g at the time of the GFM exiting CSM.

The complete control process description is as follows. The main control section determines whether the GFM operates the current limitation operation based on whether the current

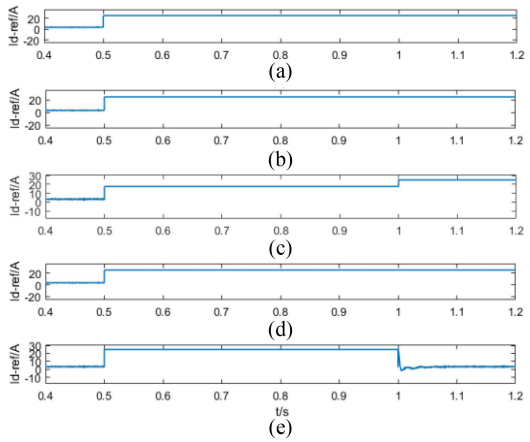

Fig. 16. d-Axis component of current reference of GFMs. (a) First strategy. (b) Second strategy. (c) Third strategy. (d) Fourth strategy. (e) Proposed strategy.

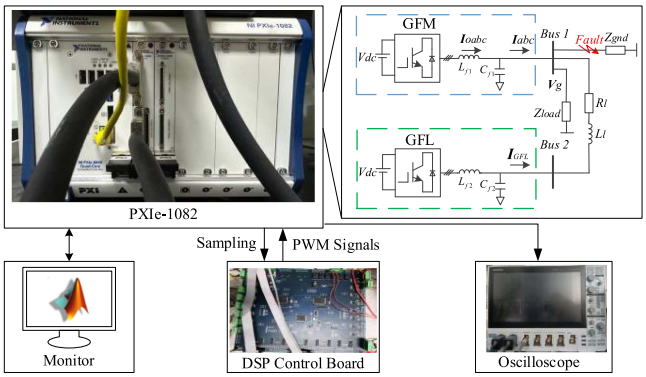

Fig. 17. HIL experiment topology.

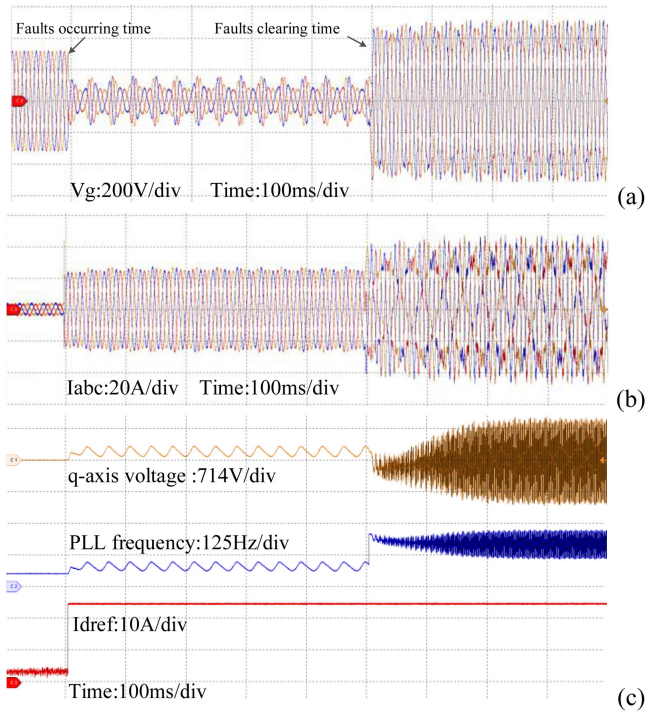

Fig. 18. Experimental results of the first strategy. (a) V_{g}. (b) I_{abc}. (c) q-Axis voltage, PLL frequency, and I_{dref}.

TABLE II
ADRs OF THE EP FOR DIFFERENT GFL CURRENT VALUES

I_{dref} (A)	The EP (x_1, x_2)	r
4	(0.63, 0)	0.89
6	(1.09, 0)	0.40
7	—	—

reference generated by the voltage loop is greater than the maximum allowable current magnitude. If $I^* \geq I_{\max}$, $S = 2$, which means that the current references are given according to the current limitation strategy in (1), i.e., $I_{dref} = I_{\max}$, $I_{qref} = 0$; $j = 0$, which is multiplied by the integrator to froze the integrator; And flag = 1, the flag changes from low potential to high potential, creating a rising edge to activate the Q-V loop to generate the voltage reference. If $I^* < I_{\max}$, $S = 1$, which means that the current references are given by the voltage control loop; $j = 1$, which is multiplied by the integrator to enable the integrator; And flag = 0, the flag changes from high potential to low potential, creating a falling edge to activate the dynamic adjustment of voltage reference section to generate the voltage reference.

V. Simulation Verification

To verify the effectiveness of the analysis and the proposed control method, the IMG shown in Fig. 1 is established using MATLAB/Simulink. The parameters are listed in Table I.

A. Effect of Different Parameters on Transient Stability

At $t = 0.5$ s, a three-phase ground fault occurs at Bus1, causing a drop in system voltage and resulting in the excessive output current of the GFM. The GFM transition from VSM to CSM under the action of current limiters. The IMG becomes a CSIM. In order to ensure system stable operation during faults, the condition of GFL active current reference I_{Ldref} is obtained based on (27) and the system parameters in Table I, which is $I_{Ldref} < 6.79$ A.

To validate the effectiveness of analysis method, change the output current of the GFL and observe whether the system can operate stably when the GFM is in CSM. At the beginning, the GFL operates at a unit power factor with the output current $I_{Ldref} = 7$ A. The GFL output current is adjusted as follows:

1) $t = 0.5$ s, $I_{Ldref} = 4$ A;
2) $t = 0.7$ s, $I_{Ldref} = 6$ A;
3) $t = 1$ s, $I_{Ldref} = 7$ A.

The output current of the GFM I_{abc}, the voltage at PCC v_{PCC}, the q-axis voltage of v_{PCC}, and the output frequency of PLL are shown in Fig. 10. The ADRs are calculated in Table II.

In Fig. 10, when the GFL output current exceeds the theoretical calculation threshold, I_{abc} oscillates. The voltage v_{PCC} is chaotic, the q-axis voltage of v_{PCC} cannot return to zero and

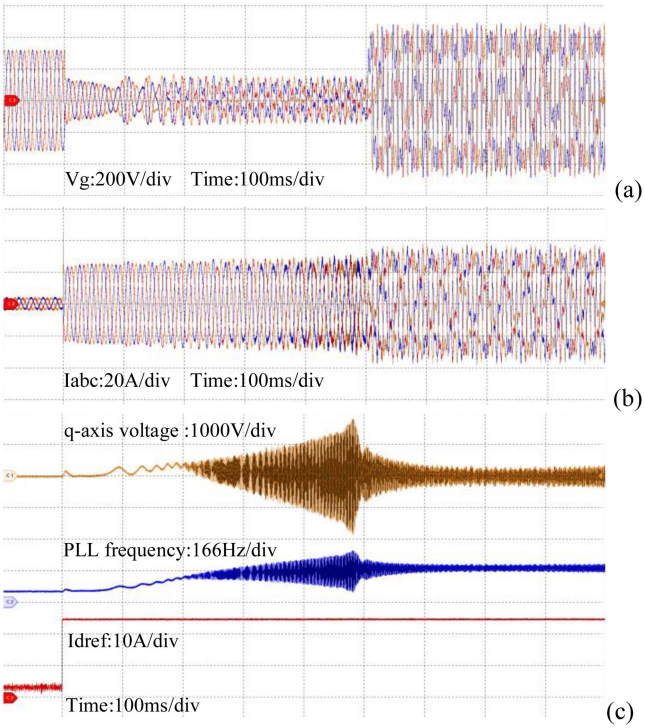

Fig. 19. Experimental results of the second strategy. (a) V_{g}. (b) I_{abc}. (c) q-Axis voltage, PLL frequency, and I_{dref}.

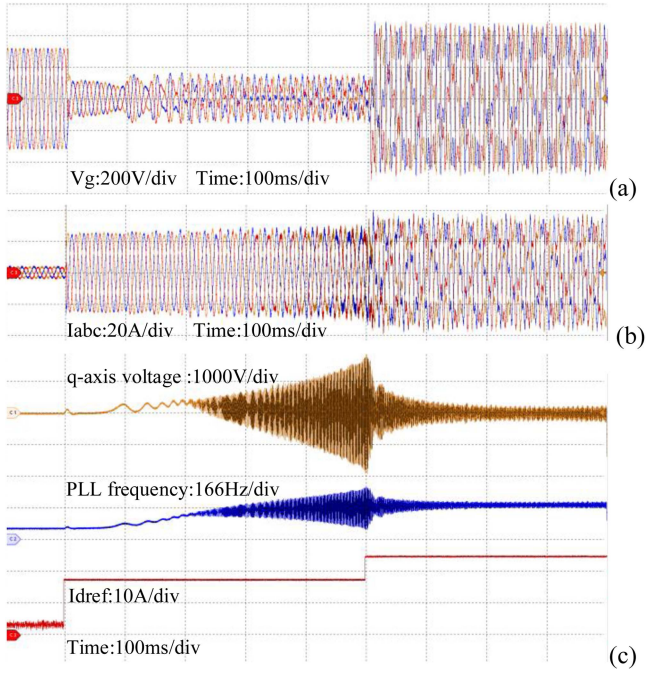

Fig. 20. Experimental results of the third strategy. (a) V_{g}. (b) I_{abc}. (c) q-Axis voltage, PLL frequency, and I_{dref}.

the output frequency of PLL is divergent and cannot return to 50 Hz, which indicates the system loses stability. Meanwhile, the value of r decreases as the output current of the GFL increases as shown in Table II, which indicates that the system strength is decreasing. Especially, when the GFL output current exceeds the theoretical calculation threshold, there are no EPs and the domain attraction's radius, which are represented by the symbol "—." The system loses stability. The system stability is consistent with the results given by the proposed stability criterion, which verifies the effectiveness of the proposed transient stability analysis method.

B. *Effectiveness of the Proposed Control Method*

To verify the feasibility and effectiveness of the proposed enhancement control method, the comparative analysis of the transient stability of the CSIM is carried out when the following control strategies are adopted during faults.

1) Variable structure PLL method proposed in [29], which freezes the integral regulator and remains the proportional regulator of PLL during faults.
2) An enhanced P-f droop control method proposed in [10], in which the q-axis component of the GFM voltage is added.
3) The current reference angle control method proposed in [17], which adjusts the current reference of the GFM.
4) The GFL adopts the proposed control method in this article, and the GFM adopts the antiwindup strategy proposed in [20], which freezes the integral regulator when the GFM operates in CSM.
5) The GFL and the GFM both adopt the proposed enhancement control method in this article.

Note that the antiwindup strategy based on the clamping method is used for the PI regulators in the first three control strategies.

At $t = 0.5$ s, a three-phase ground fault occurs at Bus1 with a duration of 500 ms. The simulation results are displayed in Figs. 11–16.

In Figs. 11–13, the first three strategies are applied. It can be seen that the system loses transient stability when the GFM transition to CSM at $t = 0.5$ s, as output current waveform of the GFM I_{abc} and the voltage waveform V_g are oscillating or chaotic, the q-axis voltage of v_{PCC} and output frequency of PLL are oscillating or divergent. As seen from Fig. 16(a)–(c), the d-axis component of the GFM current reference is shown, which reflects the GFM operation status after the fault is cleared. What is worse, after the fault is cleared at $t = 1$ s, the GFM operates the current limitation, as the current references of the GFM always remain in limitation value, which means that the GFM cannot recover from faults successfully, resulting in system instability.

In Fig. 14, the fourth strategy is adopted. It can be seen that the system is stable when GFM transition to CSM during the fault. However, after the fault is cleared, the GFM cannot restore to the normal operation as well, as the current is still saturated shown in Fig. 16(d), causing the system instability.

Meanwhile, as seen from Figs. 12 and 13, the waveforms are very similar, which means that improving the control method of the GFM has little impact on the system's transient stability during faults. It also can be verified by comparing with Figs. 11 and 14. When the GFL adopts the variable structure PLL method, although the system is unstable during faults, the voltage of Bus 1 and output frequency of PLL are oscillating rather than

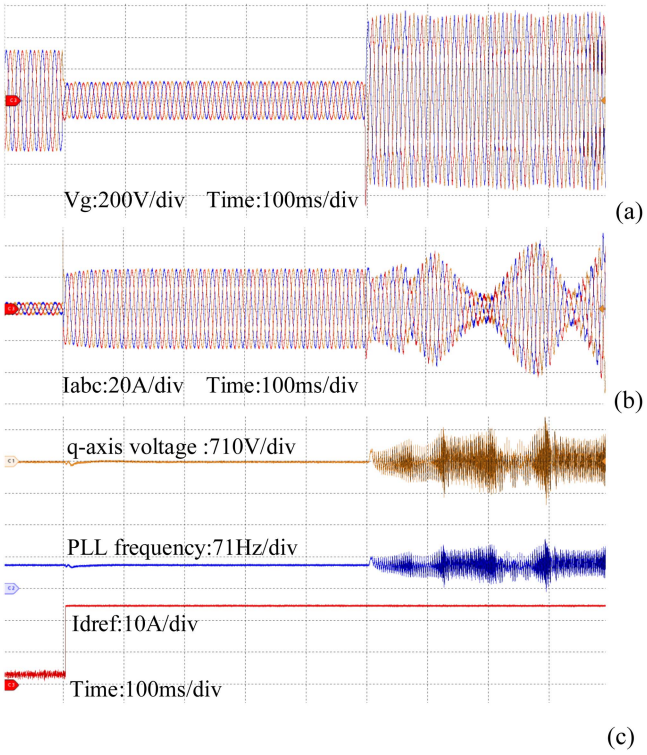

Fig. 21. Experimental results of the fourth strategy. (a) V_{g}. (b) I_{abc}. (c) q-Axis voltage, PLL frequency, and I_{dref}.

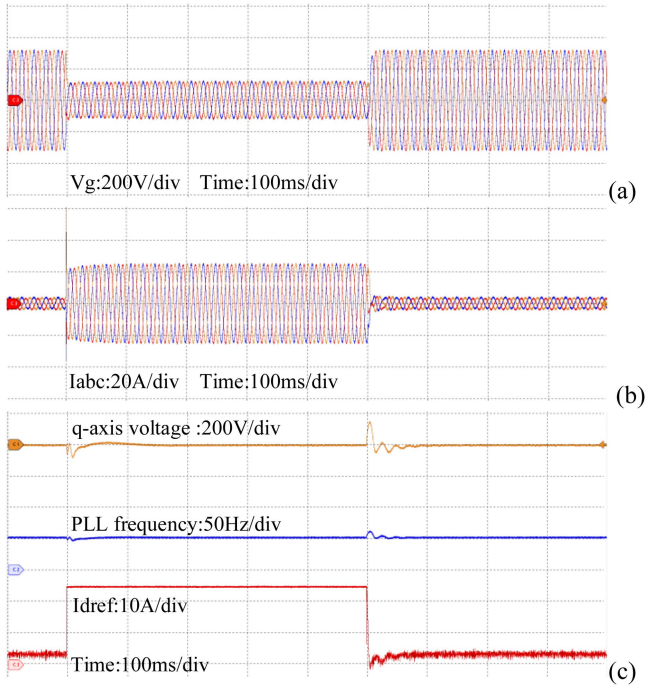

Fig. 22. Experimental results of the proposed strategy. (a) V_{g}. (b) I_{abc}. (c) q-Axis voltage, PLL frequency, and I_{dref}.

divergent, which means that the system transient stability is better than that when the GFM adopts the improvement control method. When the GFL adopts the proposed control method in this article, the system is stable when GFM transition to CSM during faults. The above analysis indicates that the system's transient stability during faults is mainly affected by GFLs.

In Fig. 15, the GFL and the GFM both adopt the proposed enhancement control method in this article. It can be seen that the system is stable when GFM transitions to CSM during faults. In addition, the GFM can successfully restore to the normal operation after the fault is cleared, as the current restores to the normal value, as shown in Fig. 16(e). These simulation results demonstrate the feasibility and effectiveness of the proposed enhancement control method.

VI. Experimental Results

In order to verify the effectiveness and superiority of the proposed analysis and enhancement method, a hardware in-the-loop (HIL) model of an IMG shown as in Fig. 1 is built. The system parameters are shown in Table I. The HIL experimental platform is shown in Fig. 17. The switching frequency is 10 kHz. The MATLAB simulation model and control program are downloaded from the monitor to the PXIe-1082. The digital signal processor samples from the PXIe-1082 and generates PWM signals. The oscilloscope is used to observe the system waveform.

A three-phase ground fault occurs at Bus1 with a duration of 500 ms. The experimental results are shown in Figs. 18–22 when the above five control strategies are adopted during faults.

As seen from Figs. 18–20, when the first three control strategies are used, the system loses transient stability during faults. As seen from Fig. 21, when the fourth strategy is adopted, the GFM cannot restore to the normal operation after the fault is cleared.

As seen from Fig. 22, when the proposed enhancement method in this article is adopted during faults, the system is stable when GFM transition to CSM during faults. In addition, the GFM can successfully restore to the normal operation after the fault is cleared, as the current restores to the normal value. Therefore, the performance of the proposed control method can be verified through the experimental results.

VII. Conclusion

In IMG, the GFM will be switched from VSM to CSM by the limitation of current under grid faults, which will exacerbate the system TSS. The instability mechanism of this phenomenon has not been studied yet. Consequently, this article has proposed a TSS analysis and enhancement method of CSIM. Compared with the existing literature works, four advantages have been found in this article as follows.

1) A large signal synchronization model of CSIM has been derived. It has revealed that the frequency interactions between GFMs and GFLs exist and the dynamic equations are entirely determined by the current outputs of GFMs and GFLs, as well as the system impedance.
2) By constructing the Lyapunov energy function, the criterion of TSS has been obtained, and the FRCR of GFLs has been derived, which provides guidance for system parameters design.

3) Based on the stability criterion, a dynamic current control method of GFLs has been proposed, which can address the absence of EPs and strengthen the transient stability.
4) In order to address the issue of the GFM fault recovery, a novel antiwindup strategy of GFMs considering system synchronization stability has been proposed. It can eliminate the impact of the sudden changes in the difference between the voltage reference and the measurement on the GFM fault recovery.

Finally, the simulation and experimental results have been provided to verify the effectiveness of the transient stability analysis and enhancement control methods.

APPENDIX

A. Derivation of (22) and (23)

It is clear that the value of $V(\tilde{x})$ is zero when $\tilde{x}_1 = \tilde{x}_2 = 0$. Since $\tilde{x}_2^2 > 0$ for all $\tilde{x}_2 \neq 0$, $V(\tilde{x}) > 0$ in the area W_1 if

$$f(\tilde{x}_1) = -A\tilde{x}_1 - B\left[cos\left(\tilde{x}_1 + \beta + \varphi_1\right) - cos\left(\beta + \varphi_1\right)\right] > 0 \tag{A1}$$

in a neighborhood around $\tilde{x}_1 = 0$.

The expression of $f'(\tilde{x}_1)$ is as follows, which is zero at $\tilde{x}_1 = 0$. Hence, $\tilde{x}_1 = 0$ is an extremum of $f(\tilde{x}_1)$

$$f'(\tilde{x}_1) = -A + B\sin\left(\tilde{x}_1 + \beta + \varphi_1\right). \tag{A2}$$

The expression of $f''(\tilde{x}_1)$ is as follows, which is a positive value at $\tilde{x}_1 = 0$

$$f''(\tilde{x}_1) = B\cos\left(\tilde{x}_1 + \beta + \varphi_1\right). \tag{A3}$$

So, the origin is the local minimum point of $V(\tilde{x})$. $V(\tilde{x})$ is positive definite in the area W_1. When $0 < \tilde{x}_1 < \pi - 2(\beta + \varphi_1)$, $f'(\tilde{x}_1) > 0$; when $-\pi - 2(\beta + \varphi_1) < \tilde{x}_1 < 0$, $f'(\tilde{x}_1) < 0$. Therefore, the previous and next extremum points of $f(\tilde{x}_1)$ are $\tilde{x}_1 = -\pi - 2(\beta + \varphi_1)$ and $\tilde{x}_1 = \pi - 2(\beta + \varphi_1)$, which are local maximums and positive values.

Based on this, the area W_1 is obtained as follows, in which $V(\tilde{x}) > 0$

$$f(\tilde{x}_1) > 0 \ \forall \tilde{x}_1 \in \left[-\pi - 2\sin^{-1}(A/B), \ \pi - 2\sin^{-1}(A/B)\right] - \{0\}. \tag{A4}$$

The time derivative of (20) is as follows:

$$\dot{V}(\tilde{x}) = -D_{eq}\tilde{x}_2^2 < 0, \quad \forall \tilde{x} \in W_2 - \{0\}. \tag{A5}$$

Since $\tilde{x}_2^2 > 0$ for all $\tilde{x}_2^2 \neq 0$, the (A5) becomes (A6) by setting $\tilde{x}_1 = 0$ in (A5), which is similar to the stability condition of EPs shown as (17)

$$D_{eq|\tilde{x}_1=0} = k_3 + \sqrt{k_4^2 + k_5^2}\sin\left(\beta + \varphi_2\right) > 0. \tag{A6}$$

Owing to $g(\tilde{x}_1) = D_{eq} = k_3 + \sqrt{k_4^2 + k_5^2}\sin(\tilde{x}_1 + \beta + \varphi_2)$ is a differentiable function. There exists a neighborhood around $\tilde{x}_1 = 0$ where $\dot{V}(\tilde{x}) < 0$. So, the origin is asymptotically stable

Because $g(\tilde{x}_1) = 0$ at $\tilde{x}_1 = \sin^{-1}(-k_3/\sqrt{k_4^2 + k_5^2}) - (\beta + \varphi_2)$. The area W_2 is obtained as follows, in which $\dot{V}(\tilde{x}) < 0$

$$g(\tilde{x}_1) > 0 \ \forall \tilde{x}_1 \in \begin{bmatrix} \sin^{-1}\left(-k_3/\sqrt{k_4^2+k_5^2}\right) - \sin^{-1}(A/B) + (\varphi_1 - \varphi_2), \\ \pi - \sin^{-1}\left(-k_3/\sqrt{k_4^2+k_5^2}\right) - \sin^{-1}(A/B) + (\varphi_1 - \varphi_2) \end{bmatrix} - \{0\}. \tag{A7}$$

REFERENCES

[1] B. Fan and X. Wang, "A lyapunov-based nonlinear power control algorithm for grid-connected VSCs," *IEEE Trans. Ind. Electron.*, vol. 69, no. 3, pp. 2916–2926, Mar. 2022.

[2] R. Wang, Q. Sun, W. Hu, Y. Li, D. Ma, and P. Wang, "SoC-based droop coefficients stability region analysis of the battery for stand-alone supply systems with constant power loads," *IEEE Trans. Power Electron.*, vol. 36, no. 7, pp. 7866–7879, Jul. 2021.

[3] L. Harnefors, J. Kukkola, M. Routimo, M. Hinkkanen, and X. Wang, "A universal controller for grid-connected voltage-source converters," *IEEE J. Emerg. Sel. Topics Power Electron.*, vol. 9, no. 5, pp. 5761–5770, Oct. 2021.

[4] R. Wang, X. Yu, Q. Sun, D. Li, Y. Gui, and P. Wang, "The integrated reference region analysis for parallel DFIGs' interfacing inductors," *IEEE Trans. Power Electron.*, vol. 39, no. 6, pp. 7632–7642, Jun. 2024.

[5] R. Rosso, X. Wang, M. Liserre, X. Lu, and S. Engelken, "Grid-forming converters: Control approaches, grid-synchronization, and future trends-a review," *IEEE Open J. Ind. Appl.*, vol. 2, pp. 93–109, Apr. 2021.

[6] B. Hu, L. Zhan, S. Sahoo, L. Chen, H. Nian, and F. Blaabjerg, "Synchronization stability analysis under ultra-weak grid considering reactive current dynamics," *IEEE Trans. Ind. Electron.*, vol. 71, no. 11, pp. 15220–15223, Nov. 2024, doi: 10.1109/TIE.2024.3370947.

[7] M. Eskandari and A. V. Savkin, "On the impact of fault ride-through on transient stability of autonomous microgrids: Nonlinear analysis and solution," *IEEE Trans. Smart Grid*, vol. 12, no. 2, pp. 999–1010, Mar. 2021.

[8] H. Xin, L. Huang, L. Zhang, Z. Wang, and J. Hu, "Synchronous instability mechanism of P-F droop-controlled voltage source converter caused by current saturation," *IEEE Trans. Power Syst.*, vol. 31, no. 6, pp. 5206–5207, Nov. 2016.

[9] M. G. Taul, X. Wang, P. Davari, and F. Blaabjerg, "Current limiting control with enhanced dynamics of grid-forming converters during fault conditions," *IEEE J. Emerg. Sel. Topics Power Electron.*, vol. 8, no. 2, pp. 1062–1073, Jun. 2020.

[10] L. Huang, H. Xin, Z. Wang, K. Wu, and J. Hu, "Transient stability analysis and control design of droop-controlled voltage source converters considering current limitation," *IEEE Trans. Smart Grid*, vol. 10, no. 1, pp. 578–591, Jan. 2019.

[11] A. D. Paquette and D. M. Divan, "Virtual impedance current limiting for inverters in microgrids with synchronous generators," *IEEE Trans. Ind. Appl.*, vol. 51, no. 2, pp. 1630–1638, Mar./Apr. 2015.

[12] T. Liu, X. Wang, F. Liu, K. Xin, and Y. Liu, "A current limiting method for single-loop voltage-magnitude controlled grid-forming converters during symmetrical faults," *IEEE Trans. Power Electron.*, vol. 37, no. 4, pp. 4751–4763, Apr. 2022.

[13] T. Qoria, F. Gruson, F. Colas, X. Kestelyn, and X. Guillaud, "Current limiting algorithms and transient stability analysis of grid-forming VSCs," *Electric Power Syst. Res.*, vol. 189, Dec. 2020, Art. no. 106726.

[14] S. Tan, H. Geng, and G. Yang, "Phillips-Heffron model for current controlled power electronic generation unit," *J. Modern Power Syst. Clean Energy*, vol. 6, no. 3, pp. 582–594, May 2018.

[15] Y. Li et. al., "PLL synchronization stability analysis of MMC-connected wind farms under high-impedance AC faults," *IEEE Trans. Power Syst.*, vol. 36, no. 3, pp. 2251–2261, May 2021.

[16] Y. Liu, H. Geng, M. Huang, and X. Zha, "Dynamic current limiting of grid-forming converters for transient synchronization stability enhancement," *IEEE Trans. Ind. Appl.*, vol. 60, no. 2, pp. 2238–2248, Mar./Apr. 2024, doi: 10.1109/TIA.2023.3305428.

[17] E. Rokrok, T. Qoria, A. Bruyere, B. Francois, and X. Guillaud, "Transient stability assessment and enhancement of grid-forming converters embedding current reference saturation as current limiting strategy," *IEEE Trans. Power Syst.*, vol. 37, no. 2, pp. 1519–1531, Mar. 2022.

[18] Y. Liu, Y. Wang, X. Liu, M. Wang, Z. Xu, and H. Liu, "Steady-state angle stability analysis of parallel grid-forming converters in current saturation mode," *IEEE Trans. Power Electron.*, vol. 38, no. 7, pp. 8039–8044, Jul. 2023.

[19] B. Fan and X. Wang, "Fault recovery analysis of grid-forming inverters with priority-based current limiters," *IEEE Trans. Power Syst.*, vol. 38, no. 6, pp. 5102–5112, Nov. 2023.

[20] T. Qoria, "Grid-forming control to achieve a 100% power electronics interfaced power transmission systems," Ph.D. dissertation, HESAM Université, Paris, France, Nov. 2020.

[21] R. Wang, X. Zhao, Q. Sun, J. Xiao, L. Zhang, and P. Wang, "Stability analysis of phase locked loops for AC microgrids with hybrid power sources," *IEEE Trans. Energy Convers.*, vol. 38, no. 2, pp. 1197–1207, Jun. 2023.

[22] Z. Wang et al., "PLL synchronization transient stability analysis of a weak-grid connected VSC during asymmetric faults," *IEEE Trans. Power Electron.*, vol. 39, no. 2, pp. 2140–2154, Feb. 2024.

[23] Z. Wang, L. Ding, X. Gao, G. Zhu, X. Wang, and V. Terzija, "Improved active current control scheme of wind energy conversion systems with PLL synchronization during grid faults," *IEEE Trans. Sustain. Energy*, vol. 14, no. 1, pp. 717–729, Jan. 2023.

[24] Z. Wang, G. Zhu, H. Wu, X. Gao, L. Ding, and X. Wang, "Current reference control scheme of voltage source converters to ensure the existence of stable equilibrium points during grid fault," *IEEE Trans. Power Electron.*, vol. 38, no. 9, pp. 10750–10765, Sep. 2023.

[25] Q. Hu, L. Fu, F. Ma, G. Wang, C. Liu, and Y. Ma, "Impact of LVRT control on transient synchronizing stability of PLL-based wind turbine converter connected to high impedance AC grid," *IEEE Trans. Power Syst.*, vol. 38, no. 6, pp. 5445–5458, Nov. 2023.

[26] X. Li et al., "Nonlinear modeling and stability analysis of grid-tied paralleled-converters systems based on the proposed dual-iterative equal area criterion," *IEEE Trans. Power Electron.*, vol. 38, no. 6, pp. 7746–7759, Jun. 2023.

[27] M. Z. Mansour, S. P. Me, S. Hadavi, B. Badrzadeh, A. Karimi, and B. Bahrani, "Nonlinear transient stability analysis of phased-locked loop-based grid-following voltage-source converters using lyapunov's direct method," *IEEE J. Emerg. Sel. Topics Power Electron.*, vol. 10, no. 3, pp. 2699–2709, Jun. 2022.

[28] X. Fu et al., "Large-signal stability of grid-forming and grid-following controls in voltage source converter: A comparative study," *IEEE Trans. Power Electron.*, vol. 36, no. 7, pp. 7832–7840, Jul. 2021.

[29] X. He, H. Geng, J. Xi, and J. M. Guerrero, "Resynchronization analysis and improvement of grid-connected VSCs during grid faults," *IEEE J. Emerg. Sel. Topics Power Electron.*, vol. 9, no. 1, pp. 438–450, Feb. 2021.

[30] S. Huang, J. Yao, J. Pei, S. Chen, Y. Luo, and Z. Chen, "Transient synchronization stability improvement control strategy for grid-connected VSC under symmetrical grid fault," *IEEE Trans. Power Electron.*, vol. 37, no. 5, pp. 4957–4961, May 2022.

[31] P. Giroux and G. Sybille, *Static Synchronous Compensator (STATCOM) Used for Midpoint Voltage Regulation on a 500kV Transmission Line*. Natick, MA, USA: MathWorks, 2006.

[32] M. Zhao, X. Yuan, J. Hu, and Y. Yan, "Voltage dynamics of current control time-scale in a VSC-connected weak grid," *IEEE Trans. Power Syst.*, vol. 31, no. 4, pp. 2925–2937, Jul. 2016.

[33] U. Markovic, O. Stanojev, P. Aristidou, E. Vrettos, D. Callaway, and G. Hug, "Understanding small-signal stability of low-inertia systems," *IEEE Trans. Power Syst.*, vol. 36, no. 5, pp. 3997–4017, Sep. 2021.

[34] N. G. Bretas and L. F. C. Alberto, "Lyapunov function for power systems with transfer conductances: Extension of the invariance principle," *IEEE Trans. Power Syst.*, vol. 18, no. 2, pp. 769–777, May 2003.

[35] J.-J. E. Slotine and W. Li, *Applied Nonlinear Control*. Englewood Cliffs, NJ, USA: Prentice-Hall, 1991.

[36] Technical Rule for Connecting Wind Farm to Power System, Chinese Standard: GB/T 19963-2011, China Electric Power Press, Beijing, China, 2011.